

# Parsimonious Model Selection for Tissue Classification: A DTI Study of Zebrafish

Raisa Z. Freidlin<sup>a,b</sup>, Michal E. Komlosh<sup>c</sup>, Murray H. Loew<sup>b</sup> and Peter J. Basser<sup>c</sup>

<sup>a</sup>TAIS, CBEL, DCB, CIT, National Institutes of Health, Bethesda, Maryland, USA;

<sup>b</sup>ECE Department, George Washington University, Washington, DC, USA;

<sup>c</sup>STBB, LIMB, NICHD, National Institutes of Health, Bethesda, Maryland, USA

## ABSTRACT

One aim of this work is to investigate the feasibility of using a hierarchy of models to describe diffusion tensor MRI data. Parsimonious model selection criteria are used to choose among different models of diffusion within tissue. Second, based on this information, we assess whether we can perform simultaneous tissue segmentation and classification. The proposed hierarchical framework used for parsimonious model selection is based on the  $F$ -test, adapted from Snedecor.

Diffusion Magnetic Resonance Microscopy (MRM) provides near-microscopic resolution without relying on a sample's optical transparency for image formation. Diffusion MRM is a noninvasive imaging technique for quantitative analysis of intrinsic features of tissues. Thus, we propose using Diffusion MRM to characterize normal tissue structure in adult zebrafish, and possibly subtle anatomical or structural differences between normals and knockouts.

Both numerical phantoms and diffusion weighted image (DWI) data obtained from adult zebrafish are used to test this model selection framework.

**Keywords:** DTI, diffusion tensor, MRI, hierarchical, parsimonious, model selection

## 1. INTRODUCTION

The zebrafish is an important model organism in developmental biology; in the past two decades it has become the most important model organism for developmental biology and genomics research in vertebrates.<sup>1-5</sup> Because it is optically transparent during the embryonic and early juvenile stages, it is amenable to study via powerful optical techniques. Primarily, confocal fluorescence microscopy is used to identify genes responsible for cell function, and tissue and organ formation in normal development, as well as to assess structural alterations that can be induced by "knocking out" these genes, which can sometimes be related to known diseases or developmental disorders. However, as the zebrafish approaches adulthood, it grows larger and becomes optically turbid so that these powerful optical microscopy techniques no longer work. Consequently, genetic studies in zebrafish are effectively limited to examining changes in form and function during the organism's early embryonic development. However, many have hypothesized that certain genes in zebrafish remain silent during periods of early growth, only to be expressed in the adult stages, leading to possible disease, dysfunction or dysregulation in maturity. Such studies have not been undertaken in zebrafish owing to the limitations discussed above.

*In vivo* Magnetic Resonance Microscopy (MRM) methods are increasingly being applied to studying microstructure and microanatomy in a variety of animal models, such as rats and mice. However, there are only a few MRM studies on adult zebrafish. Although the spatial resolution of MRM is not presently comparable to high-resolution light microscopy, it has several desirable attributes: it is noninvasive, provides quantitative information on molecular dynamics, and generates quantitative maps of the spatial distribution of specific molecules or parameters describing different relaxation processes.

We investigated *in vitro* MRM imaging techniques to study adult zebrafish at the point in development when the tissue becomes optically turbid and is no longer amenable to analysis using conventional optical microscopy

---

Further author information: Send correspondence to Raisa Z. Freidlin, E-mail: raisa@helix.nih.gov, Telephone: 1-301-402-2788

methods. Further developments might extend the gestational age that the zebrafish model could be studied, and open the possibility of discovering mutant genotypes that are associated with phenotypic alterations linked to disease or abnormal development later in life.

Diffusion Tensor Magnetic Resonance Imaging<sup>6</sup> (DT-MRI) is a noninvasive imaging technique for quantitative analysis of intrinsic features of tissues. DT-MRI has been applied to study the structural organization of skeletal muscles,<sup>7</sup> brain,<sup>8</sup> spinal cord,<sup>9</sup> peripheral nerves,<sup>10</sup> intervertebral discs,<sup>11</sup> and heart.<sup>12,13</sup> Based on its extensive use, it is increasingly important to develop new tools for efficient and accurate tissue analysis and segmentation of DT-MRI data. Most work to date has been to characterize the Trace of the diffusion tensor,  $Tr$ , the Fractional Anisotropy,  $FA$ , and the fiber orientation of tissue. Comparably little has been done to identify the underlying microstructure and microstructural models appropriate for each voxel.

Tissue segmentation and classification are the most challenging tasks in DT image analysis. Segmentation separates acquired data into objects, while tissue classification generates meaningful regions of interest. Here we examine whether parsimonious model selection criteria applied to a hierarchy of diffusion models can provide simultaneous tissues segmentation and classification based on the underlying diffusion properties.

A hierarchy of diffusion models and a statistical hypothesis testing framework were used in the context of the first MR measurement of the translational diffusion tensor,<sup>6</sup> to determine whether proton diffusion was isotropic or anisotropic in water and in a skeletal muscle phantom. Because this study used diffusion spectroscopy sequences with data obtained at a high Signal to Noise Ratios ( $SNR$ ), it was not clear whether such approaches would work at the  $SNR$  of clinical or animal images or would behave reliably from voxel to voxel within an image volume. Subsequently, Basser proposed using diffusion models with different degrees of symmetry to describe diffusion transport in tissue.<sup>14,15</sup>

In this work we test the appropriateness and relative efficiency of four predefined diffusion models: Currently, there are a number of known diffusion models (see examples below) that incorporate *a priori* knowledge of the different types of tissue paradigms:

1. isotropic: No preferred diffusion direction detectable
2. anisotropic:
  - (a) general anisotropic
  - (b) prolate
  - (c) oblate

The method for parsimonious model selection used here to process zebrafish data is based on the  $F$ -test.<sup>16</sup>

## 2. THEORY

### 2.1. Diffusion Tensor Imaging

Stejskal and Tanner<sup>17</sup> showed that the relationship between observed signal attenuation due to applying diffusion-weighted gradient gradients along different directions can be described by

$$S(\mathbf{G}) = S(0)e^{-bD}, \tag{1}$$

where  $S(\mathbf{G})$  is observed signal,  $S(0)$  is a signal in the absence of the diffusion-weighted gradient,  $D$  is the apparant diffusion coefficient, and  $b$  is computed by:

$$b = \gamma^2 G_i^2 \delta^2 \left[ \Delta - \frac{\delta}{3} \right], \tag{2}$$

where  $G_i$  is the magnitude of the diffusion-weighted gradient applied in  $i^{\text{th}}$  direction with duration  $\delta$ , and  $\Delta$  is the diffusion time. However, Eq. 1 characterizes diffusion only in one dimension. Diffusion Tensor Imaging (DTI)

technique<sup>6</sup> describes water molecule diffusion in three dimensional space, thus providing insightful information about structure and orientation of underlying tissue. For DTI, Eq. 1 takes the following form:

$$S(\mathbf{G}) = S(0)e^{-\mathbf{b}:\mathbf{D}}, \quad (3)$$

where  $\mathbf{D}$  is a symmetric (3x3) 2nd-order diffusion tensor that has a form:

$$\mathbf{D} = \begin{bmatrix} D_{xx} & D_{xy} & D_{xz} \\ D_{xy} & D_{yy} & D_{yz} \\ D_{xz} & D_{yz} & D_{zz} \end{bmatrix}. \quad (4)$$

Diagonal elements of the diffusion tensor,  $\mathbf{D}$ , are proportional to the diffusion rate in the collinear directions, while correlations in displacements along orthogonal directions are represented by off-diagonal elements. Since  $\mathbf{D}$  is symmetric, its six independent elements are sufficient to describe Gaussian molecular diffusivity in all three dimensions. Furthermore,  $\mathbf{D}$  is positive definite and can be represented by:

$$\mathbf{D}\mathbf{E} = \mathbf{E}\Lambda \text{ or } \mathbf{D} = \mathbf{E}\Lambda\mathbf{E}^{-1} = \mathbf{E}\Lambda\mathbf{E}^T, \quad (5)$$

$$\mathbf{E} = [\epsilon_1; \epsilon_2; \epsilon_3] \text{ and } \Lambda = \begin{bmatrix} \lambda_1 & 0 & 0 \\ 0 & \lambda_2 & 0 \\ 0 & 0 & \lambda_3 \end{bmatrix}, \quad (6)$$

where  $\mathbf{E}$  is the matrix with orthonormal eigenvectors as columns, and  $\Lambda$  is the diagonal matrix containing their corresponding eigenvalues. It was first suggested in<sup>18</sup> that in fibrous anisotropic media the eigenvector,  $\epsilon_1$ , associated with the largest eigenvalue,  $\lambda_1$ , coincides with the tissue's dominant fiber-tract axis, while the two remaining eigenvectors,  $\epsilon_2$  and  $\epsilon_3$ , define the transverse plane. For the general anisotropic model a typical observation is that  $\lambda_1 > \lambda_2 > \lambda_3$ .

It has been shown that anisotropic tissues such as skeletal muscle<sup>7</sup> and nerve white matter,<sup>19</sup> are often cylindrically symmetric having a prolate diffusion ellipsoid, i.e.,  $\lambda_1 > \lambda_2 \approx \lambda_3$ . For an oblate diffusion ellipsoid, cylindrical symmetry described as:  $\lambda_1 \approx \lambda_2 > \lambda_3$ . For both prolate and oblate models, the number of independent parameters required to characterize  $\mathbf{D}$  can be reduced from seven to five.<sup>20</sup> The diffusion tensors for both transversely isotropic models can be described by:<sup>21,22</sup>

$$\mathbf{D}_{o/p}(\alpha, \beta, \theta, \varphi) = \alpha\epsilon_{o/p}(\theta, \varphi)\epsilon_{o/p}(\theta, \varphi)' + \beta\mathbf{I}, \quad (7)$$

where  $\epsilon_{o/p}(\theta, \varphi) = (\sin\theta\cos\varphi, \sin\theta\sin\varphi, \cos\theta)'$  and  $\mathbf{I}$  is the 3x3 identity matrix. Coefficients  $\alpha$  and  $\beta$  for the oblate and prolate models can be related to the eigenvalues and eigenvectors of the diffusion tensor as follows:

$$\begin{aligned} \text{Oblate : } \lambda_1 = \lambda_2 &\Rightarrow \alpha = \lambda_3 - \lambda_2, \beta = \lambda_2, \epsilon_{o/p}(\theta, \varphi) = \epsilon_3; \\ \text{Prolate : } \lambda_2 = \lambda_3 &\Rightarrow \alpha = \lambda_1 - \lambda_2, \beta = \lambda_2, \epsilon_{o/p}(\theta, \varphi) = \epsilon_1; \end{aligned} \quad (8)$$

The simplest model is that of isotropy. While anisotropic medium requires six independent parameters to describe molecular displacement, only one scalar diffusion coefficient,  $D$ , is sufficient to describe isotropy, so Eq. 3 can be reduced to:

$$S(\mathbf{G}) = S(0)e^{-b\hat{D}}, \quad (9)$$

where  $b = b_{xx} + b_{yy} + b_{zz}$ , and  $\hat{D}$  is an estimated apparent diffusion coefficient. The isotropic diffusion tensor has the form:

$$\mathbf{D} = \hat{D}\mathbf{I}. \quad (10)$$

Eq. 10 is a special case of Eq. 7 in which  $\alpha = 0$  and  $\beta = \hat{D}$ . The hierarchical approach will select between parsimonious models which are given by Eqs 4, 7, and 10.

## 2.2. Parameter estimation for the different models

The diffusion tensor is estimated by non-linear least square minimization method, proposed by Koay et al.<sup>23</sup> The design matrix,  $\mathbf{B}$ , consists of a list of  $\mathbf{b}$ -matrix elements, written as row vectors, for a series of  $n$  trials:

$$\mathbf{B} = \begin{bmatrix} b_{x_1}^2 & b_{y_1}^2 & b_{z_1}^2 & 2b_{x_1y_1} & 2b_{x_1z_1} & 2b_{y_1z_1} & -1 \\ b_{x_2}^2 & b_{y_2}^2 & b_{z_2}^2 & 2b_{x_2y_2} & 2b_{x_2z_2} & 2b_{y_2z_2} & -1 \\ \vdots & \vdots & \vdots & \vdots & \vdots & \vdots & \vdots \\ \vdots & \vdots & \vdots & \vdots & \vdots & \vdots & \vdots \\ b_{x_n}^2 & b_{y_n}^2 & b_{z_n}^2 & 2b_{x_ny_n} & 2b_{x_nz_n} & 2b_{y_nz_n} & -1 \end{bmatrix}, \quad (11)$$

and  $\hat{\mathbf{D}}$  is the estimated diffusion tensor for the general anisotropic model written as a  $(7 \times 1)$  column vector. Here we estimate six independent parameters of  $\mathbf{D}$  and the log of the signal in the absence of the diffusion-weighted gradient,  $\log[S(0)]$ :

$$\hat{\mathbf{D}} = [D_{xx}, D_{yy}, D_{zz}, D_{xy}, D_{xz}, D_{yz}, \log[S(0)]]', \quad (12)$$

For cylindrically symmetric oblate and prolate models the number of free parameters we estimate is reduced from 7 to 5:

$$[\alpha, \beta, \theta, \varphi, \log[S(0)]]', \quad (13)$$

where the initial guesses of  $\alpha, \beta, \theta, \varphi$  are obtained from the previous estimate of the eigenvalues and eigenvectors of  $\mathbf{D}$ :

$$\begin{aligned} \text{Oblate} : \lambda_1 \approx \lambda_2 &\Rightarrow \alpha = \lambda_3 - \left(\frac{\lambda_1 + \lambda_2}{2}\right), \beta = \frac{\lambda_1 + \lambda_2}{2}, \epsilon_{o/p}(\theta, \varphi) = \epsilon_3; \\ \text{Prolate} : \lambda_2 \approx \lambda_3 &\Rightarrow \alpha = \lambda_1 - \left(\frac{\lambda_2 + \lambda_3}{2}\right), \beta = \frac{\lambda_2 + \lambda_3}{2}, \epsilon_{o/p}(\theta, \varphi) = \epsilon_1; \end{aligned}$$

For the isotropic model the number of unknown parameters is 2:

$$[\hat{D}, \log[S(0)]]'. \quad (14)$$

Once the elements of  $\hat{\mathbf{D}}$  are estimated for all four models, we can derive the corresponding residual sum of squares for each model as:

$$RSS_j = \sum_{i=1}^n \left( S_i(\mathbf{G}) - e^{-\mathbf{B}_i \hat{\mathbf{D}}} \right)^2, \quad (15)$$

where  $RSS_j = \{RSS_T, RSS_P, RSS_O, RSS_I\}$  and  $\mathbf{B}_i$  is the  $i^{\text{th}}$  row of the design matrix,  $\mathbf{B}$ .

With these definitions we are interested to know whether one could select the model which would most faithfully describe the acquired data while having the fewest unknown parameters.

## 2.3. Hierarchical parsimonious model selection

The proposed hierarchical scheme for parsimonious model selection is based on multivariate  $F$ -tests. The three steps for this approach are (Fig. 1)

1. ensure that the estimated diffusion tensor passes a  $\chi^2$  goodness-of-fit test;
2. apply an  $F$ -test to differentiate between isotropic and anisotropic models with 2 and 7 unknown parameters, respectively;
3. apply an  $F$ -test to evaluate presence of transverse isotropy or cylindrical symmetry (5 free parameters);

The multivariate  $F$ -statistic is defined as:

$$F_0 = \frac{(RSS_R - RSS_T)/(fp_T - fp_R)}{(RSS_T)/(n - fp_T)}, \quad (16)$$

where  $fp_T = 7$  and  $fp_R$  a free parameters in the general anisotropic (full tensor) and reduced (prolate or oblate for which  $fp_R = 5$ , and isotropic  $fp_R = 2$ ) models,  $n$  is the number of experimental data points, and  $RSS_R$  and  $RSS_T$  are the residual sum of squares for the reduced (prolate/oblate/isotropic) and full tensor models.

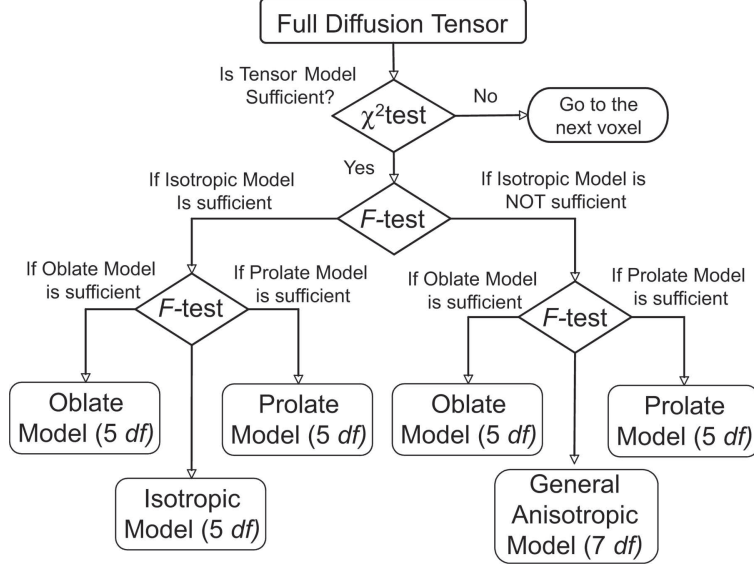


Figure 1: Schematic hierarchical model selection approach.

### 3. METHODS

#### 3.1. Monte Carlo Simulations

Since the complex MR signal is measured through a quadrature detector, it can be represented by the real and imaginary components (Eq. 17).

$$S = S_{Re} + iS_{Im} \quad (17)$$

One of the ways to simulate thermal noise present in the MR scanner, is to assume that the noise in both channels is independent and normally distributed with mean zero and standard deviation,  $\sigma$  (Eq. 18)<sup>24,25</sup>

$$S = I_0 + N_{Re} + iN_{Im}, \quad (18)$$

where  $I_0$  is the true signal.

Given this, Monte Carlo simulations were performed by adding randomly generated Gaussian noise,  $Nrand$ , to the real and imaginary components independently. Diffusion weighted images are magnitude images. They are calculated using Eq 19 .

$$DWI = \sqrt{DWI_{Re}^2 + DWI_{Im}^2}, \quad (19)$$

where

$$\begin{aligned} DWI_{Re} &= I_0 e^{-\mathbf{b} \cdot \mathbf{D}} + I_0 / SNR \cdot Nrand \\ DWI_{Im} &= I_0 / SNR \cdot Nrand. \end{aligned}$$

To validate the parsimonious model selection approach, synthetic phantoms (Fig. 2a)) were generated by varying the fractional anisotropy,  $FA=[0.2 : 0.1 : 1.0]$ , and signal to noise ratio,  $SNR=[5 : 2 : 23]$ , for a fixed signal intensity, ( $I_0=1000$ ). Trace of  $\mathbf{D}$ ,  $Tr$ , were set to  $2100 \times 10^{-6} \text{ mm}^2/\text{sec}$  and  $2500 \times 10^{-6} \text{ mm}^2/\text{sec}$  for white and gray matter respectively, which are typical values in brain tissue.

The  $\mathbf{b}$ -matrix was calculated with the imaging parameters described in the Adult Zebrafish Imaging Experiments subsection.

The hierarchical framework for parsimonious model selection was applied to the set of thirty-one reconstructed diffusion-weighted images with ten unweighed images.

### 3.2. Adult Zebrafish Imaging Experiments

Diffusion Weighted (DW) images of an adult zebrafish were performed<sup>26</sup> on a 7T Vertical bore Bruker (Billerica, MA) Oxford Instruments 81 mm Microimaging MRI System equipped with a Micro2.5 microscopy probe (15mm solenoid coil) with 950 mT/m 3-axis gradients. Samples were positioned in a custom-made holder in a 15mm glass tube filled with MR-compatible perfluoropolyether oil (“Fomblin”). DWIs were obtained using a standard PGSE DWI sequence with pulse duration  $\delta = 1.5$  ms, diffusion time  $\Delta = 25$  ms, TR = 3000 ms, and TE = 34 ms. Other imaging parameters were: in-plane resolution  $94 \times 94 \mu\text{m}^2$ , slice thickness = 1 mm, number of averages:  $n = 6$ .

Forty-one DWIs per slice were acquired during twenty-six hours of scanning. Thirty-one of these DWIs were attenuated by diffusion gradients  $\mathbf{G} = (G_x, G_y, G_z)$  and ten were not attenuated ( $|\mathbf{G}| = 0$ ). In each direction the maximum diffusion gradient strength was set to 500 mT/m. At each voxel location in the raw image, the apparent diffusion tensor,  $\hat{\mathbf{D}}$ , was estimated. Tensor-derived parameters, such as the principal directions,  $\epsilon_1$ ,  $\epsilon_2$ , and  $\epsilon_3$ , and the corresponding principal diffusivities,  $\lambda_1$ ,  $\lambda_2$ , and  $\lambda_3$ , were estimated and passed to the parsimonious model selection algorithm

## 4. RESULTS

### 4.1. Monte Carlo Simulations

The results of hierarchical framework for parsimonious model selection at  $SNR=9$  and 21 are shown in Figs. 2b) and c) respectively.

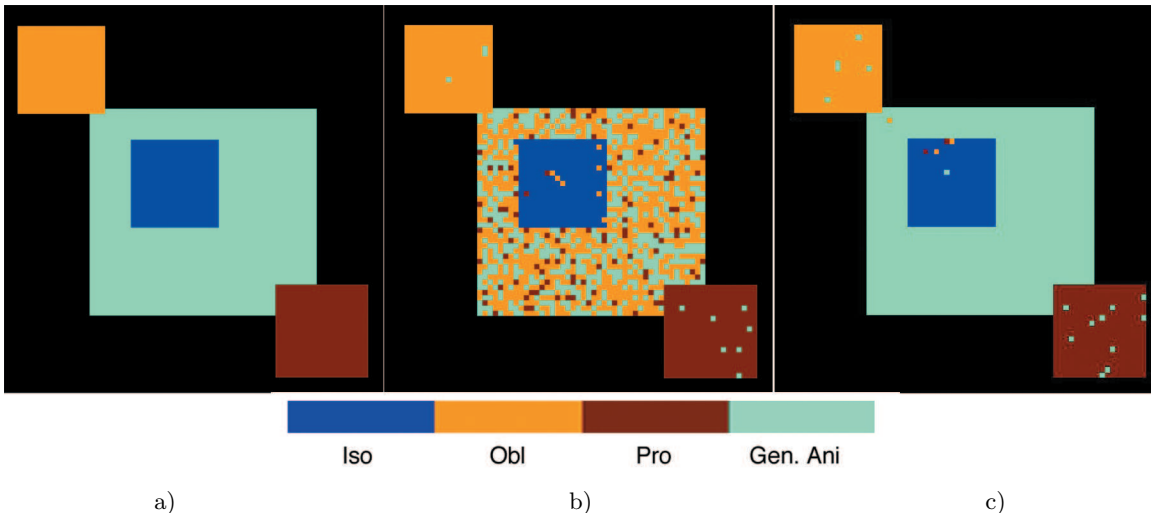


Figure 2: a) Noise-free simulated phantom; Model selection results at b)  $SNR=9$  and c)  $SNR=21$

Model selection performance results are presented in Fig. 3). It can be seen that significant improvement in the general anisotropic model regions is achieved at  $SNR=21$  and  $FA$  greater than 0.8, while oblate and prolate models performed consistently for both  $SNRs$  at  $FA$  greater than 0.6. The isotropic model selection showed consistent results for the True Positive counts at  $SNRs = 9$  and 21 with success rate of 96% and 98%, respectively (Table 1, where each column of the confusion matrix represents the true model, and each row represents the results of the parsimonious model classification). The same can be observed for the oblate and prolate models (with success rates 99% and 97%, respectively). However, for the anisotropic model the True Positive counts improve from 38% at  $SNR=9$  to 100% at  $SNR=21$ .

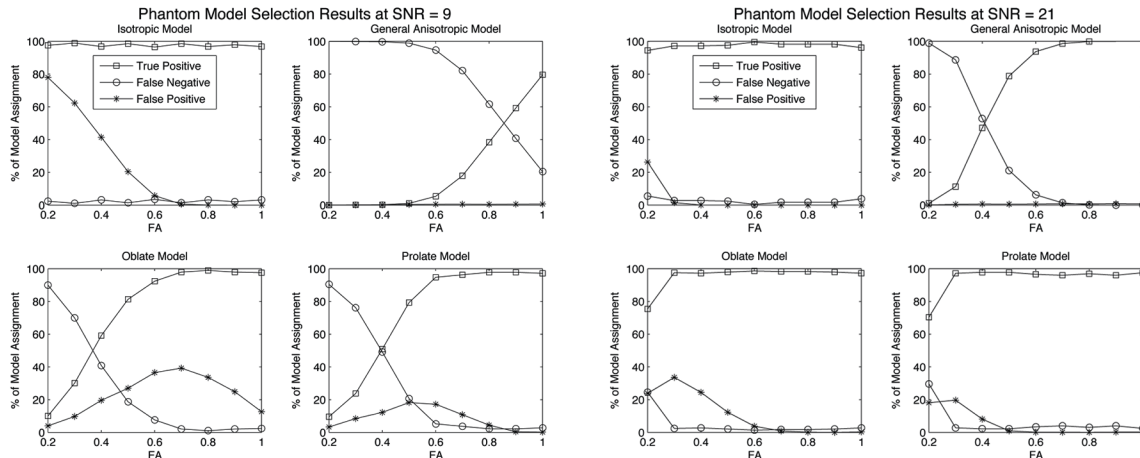


Figure 3: Results for the phantom with  $SNR=9$  and 21.

Table 1: Confusion matrix summarizes the possible misclassification errors that arise when using the model selection framework. The left column refers to the true model and the top row corresponds to the assigned model.

Model Selection Results  $SNR=9$

	Iso	Ani	Obl	Pro
Iso	96.9	0	2.4	0.7
Ani	0.1	38.4	54.4	7.1
Obl	0	1.0	99.0	0
Pro	0	2.2	0	97.8

Model Selection Results  $SNR=21$

	Iso	Ani	Obl	Pro
Iso	98.2	0.3	0.7	0.7
Ani	0	99.9	0.1	0
Obl	0	1.7	98.3	0
Pro	0	3.1	0	97.9

## 4.2. DTI Experiment on Adult Zebrafish

Fig. 4a) shows the  $T_2$ -weighted amplitude image and b) the orientationally-averaged mean diffusivity map ( $\langle \mathbf{D} \rangle = \text{Trace}/3$ ) in a slice of adult zebrafish. The amplitude image and the  $\langle \mathbf{D} \rangle$  map delineate different muscle groups consistent with histology. Also, regions appearing bright in the amplitude image appear dark in  $\langle \mathbf{D} \rangle$  map. Fig. 4c) is the direction-encoded color map in which muscle fiber groups are also easily discernible. The bluish color in the muscle groups indicates fibers pointing into the page, consistent with known anatomy. Moreover, the spinal cord is clearly visible along the central line. Also noteworthy are radially oriented structures near the skin in Fig. 4c).

The results of the parsimonious model selection are shown in Fig. 5. The hierarchical approaches showed consistency in selecting the prolate model in areas corresponding to skeletal muscles and the oblate model near the skin and at interfaces between tissue types. Three-dimensional visualization (Fig. 6) from the model map for 8 slices shows the location of prolate structures from the front and back of an adult zebrafish.

## 5. DISCUSSION AND CONCLUSIONS

This work shows the feasibility of using a parsimonious model selection criterion to obtain the most appropriate diffusion model within each voxel of an imaging volume. Since residuals are normally distributed, and the variance of each measurement is unchanging (homoscedasticity) we can safely use this hypothesis testing formalism to test one model against another. This voxel-by-voxel segmentation approach makes statistical hypothesis testing less susceptible to grouping voxels with different variances in the tensor and tensor-derived estimates.<sup>27</sup> In addition, since the proposed approach uses the information from the entire diffusion tensor its performance in tissue segmentation and classification is improved comparing to other commonly used techniques, which are based on the diffusion-derived scalars, such as  $FA$  and  $Tr$ . Furthermore, the  $F$ -test is more robust than the frequently used  $t$ -test, since it is less sensitive to the variance estimation and the bias due to sorting the eigenvalues.<sup>25,28</sup>

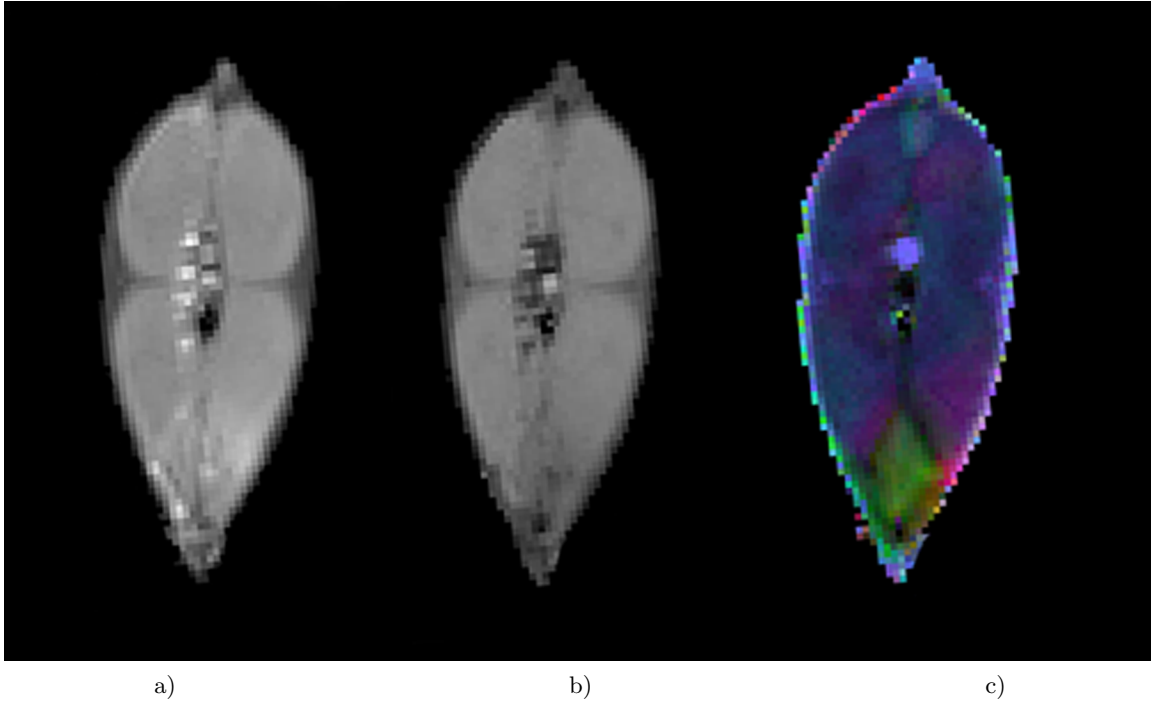


Figure 4: Adult zebrafish images: a) Amplitude; b) Trace; c) DTI colormap: red - left to right direction, green - up and down direction, blue - through the plane.

The results of the phantom simulations increase our confidence in our model selection schemes based upon statistical hypothesis tests. This approach can be successfully used with *ex vivo* data where only background noise is present. Nevertheless, providing that the conditions for normally distributed residuals and stable variances for DWI in time are met, this analysis pipeline could be extended to *in vivo* data as well. However, artifacts, such as physiological noise, motion, eddy current distortion, etc., may be significant and should be corrected prior to performing model selection. The maps produced by the proposed parsimonious model selection schemes provide useful information about the underlying tissue microstructure in each voxel. Our expectation is that these model selection procedures may lead to improvements in automatic region of interest (ROI) delineation and classification of tissue types in DT-MRI volume data sets.

Due to the simplicity and speed of implementing  $F$ -tests it is feasible to apply this framework to large DWI data sets routinely encountered in high resolution microscopic DT-MRI studies or in clinical DT-MRI applications.

### Acknowledgments

RZF Kenneth Kempner for his support and encouragement on this work. The authors would like to thank Drs. Carlo Pierpaoli, Uri Nevo, Yaniv Assaf and Marty Lizak for helpful discussions throughout this study and Liz Salak for editing this paper. This research was supported by the Intramural Research Program of the National Institute of Child Health and Development (NICHD) and the Center for Information Technology (CIT), National Institutes of Health, Bethesda, Maryland.

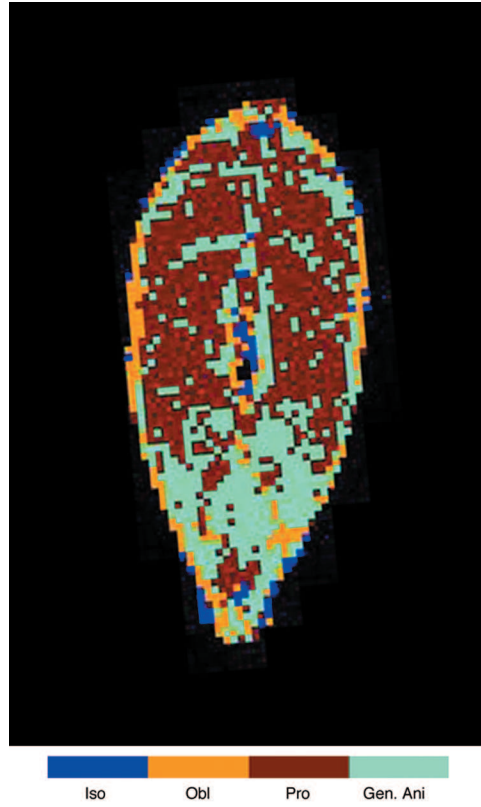


Figure 5: Adult zebrafish model maps.

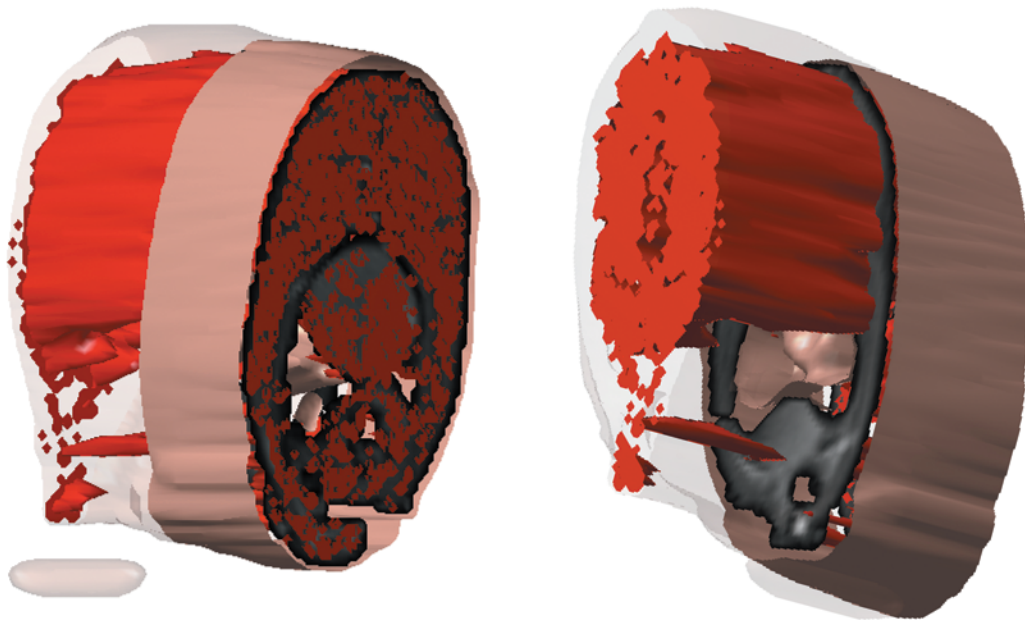


Figure 6: Model map 3D visualization of the prolapse structures from the front and back of an adult zebrafish.

## REFERENCES

1. A. Amores, A. Force, Y. L. Yan, L. Joly, C. Amemiya, A. Fritz, R. K. Ho, J. Langeland, V. Prince, Y. L. Wang, M. Westerfield, M. Ekker, and J. H. Postlethwait, "Zebrafish hox clusters and vertebrate genome evolution.," *Science* **282**, pp. 1711–1714, Nov 1998.
2. W. Driever, D. Stemple, A. Schier, and L. Solnica-Krezel, "Zebrafish: genetic tools for studying vertebrate development.," *Trends Genet* **10**, pp. 152–159, May 1994.
3. M. C. Fishman, "Genomics. Zebrafish—the canonical vertebrate.," *Science* **294**, pp. 1290–1291, Nov 2001.
4. J. H. Postlethwait and W. S. Talbot, "Zebrafish genomics: from mutants to genes.," *Trends Genet* **13**, pp. 183–190, May 1997.
5. J. H. Postlethwait, Y. L. Yan, M. A. Gates, S. Horne, A. Amores, A. Brownlie, A. Donovan, E. S. Egan, A. Force, Z. Gong, C. Goutel, A. Fritz, R. Kelsh, E. Knapik, E. Liao, B. Paw, D. Ransom, A. Singer, M. Thomson, T. S. Abduljabbar, P. Yelick, D. Beier, J. S. Joly, D. Larhammar, F. Rosa, M. Westerfield, L. I. Zon, S. L. Johnson, and W. S. Talbot, "Vertebrate genome evolution and the zebrafish gene map.," *Nat Genet* **18**, pp. 345–349, Apr 1998.
6. P. J. Basser, J. Mattiello, and D. LeBihan, "Estimation of the effective self-diffusion tensor from the NMR spin echo.," *J Magn Reson B* **103**, pp. 247–254, Mar 1994.
7. U. Sinha and L. Yao, "In vivo diffusion tensor imaging of human calf muscle.," *J Magn Reson Imaging* **15**, pp. 87–95, Jan 2002.
8. C. Pierpaoli, P. Jezzard, P. J. Basser, A. Barnett, and G. D. Chiro, "Diffusion tensor MR imaging of the human brain.," *Radiology* **201**, pp. 637–648, Dec 1996.
9. C. Clark and D. Werring, "Diffusion tensor imaging in spinal cord: methods and applications - a review.," *NMR Biomed* **15**(7-8), pp. 578–586, 2002.
10. A. G. Filler, M. Kliot, F. A. Howe, C. E. Hayes, D. E. Saunders, R. Goodkin, B. A. Bell, H. R. Winn, J. R. Griffiths, and J. S. Tsuruda, "Application of magnetic resonance neurography in the evaluation of patients with peripheral nerve pathology.," *J Neurosurg* **85**, pp. 299–309, Aug 1996.
11. E. W. Hsu and L. A. Setton, "Diffusion tensor microscopy of the intervertebral disc annulus fibrosus.," *Magn Reson Med* **41**, pp. 992–999, May 1999.
12. J. Dou, T. G. Reese, W.-Y. I. Tseng, and V. J. Wedeen, "Cardiac diffusion MRI without motion effects.," *Magn Reson Med* **48**, pp. 105–114, Jul 2002.
13. T. G. Reese, R. M. Weisskoff, R. N. Smith, B. R. Rosen, R. E. Dinsmore, and V. J. Wedeen, "Imaging myocardial fiber architecture in vivo with magnetic resonance.," *Magn Reson Med* **34**, pp. 786–791, Dec 1995.
14. P. Basser, "Testing for and exploiting microstructural symmetry to characterize tissues via diffusion tensor MRI," in *ISMRM Fourth Scientific Meeting*, **2**, p. 1323, 1996.
15. D. Shrager, D. K. Jones, S. Pajevic, P. Munson, and P. J. Basser, "When is a Gaussian displacement distribution adequate to describe water diffusion in tissues?," in *ISMRM Workshop on Diffusion MRI: Biophysical Issues: What can we measure?*, pp. 21–25, 2002.
16. G. Snedecor and W. Cochran, *Statistical Methods*, Blackwell Publishing, 8th ed., 1989.
17. E. Stejskal and J. Tanner, "Spin diffusion measurements: Spin echoes in the presence of a time-dependent field gradient," *J Chem Phys* **42**, pp. 288–292, January 1966.
18. P. J. Basser, J. Mattiello, and D. LeBihan, "MR diffusion tensor spectroscopy and imaging.," *Biophys J* **66**, pp. 259–267, Jan 1994.
19. J. Coremans, R. Luybaert, F. Verhelle, T. Stadnik, and M. Osteaux, "A method for myelin fiber orientation mapping using diffusion-weighted MR images.," *Magn Reson Imaging* **12**(3), pp. 443–454, 1994.
20. E. W. Hsu and S. Mori, "Analytical expressions for the NMR apparent diffusion coefficients in an anisotropic system and a simplified method for determining fiber orientation.," *Magn Reson Med* **34**, pp. 194–200, Aug 1995.
21. C. Westin, S. Peled, H. Gudbjartsson, R. Kikinis, and F. Jolesz, "Geometrical diffusion measures for MRI tensor basis analysis," in *ISMRM Fifth Scientific Meeting*, **3**, p. 1742, 1997.
22. D. Alexander, *An introduction to computational diffusion MRI: The diffusion tensor and beyond*, Visualization and Image Processing of Tensor Fields, New York: Springer, 2005.

23. C. G. Koay, L.-C. Chang, J. D. Carew, C. Pierpaoli, and P. J. Basser, "A unifying theoretical and algorithmic framework for least squares methods of estimation in diffusion tensor imaging.," *J Magn Reson* **182**, pp. 115–125, Jul 2006.
24. R. M. Henkelman, "Measurement of signal intensities in the presence of noise in MR images.," *Med Phys* **12**(2), pp. 232–233, 1985.
25. C. Pierpaoli and P. J. Basser, "Toward a quantitative assessment of diffusion anisotropy.," *Magn Reson Med* **36**, pp. 893–906, Dec 1996.
26. R. Z. Freidlin, H. D. Morris, F. Horkay, C. Pierpaoli, R. Toyama, I. B. Dawid, and P. J. Basser, "Diffusion tensor MR Microscopy in adult zebrafish.," in *Proc. ISMRM, Kyoto*, 2004.
27. J. D. Carew, C. G. Koay, G. Wahba, A. L. Alexander, M. E. Meyerand, and P. J. Basser, "The asymptotic behavior of the nonlinear estimators of the Diffusion Tensor and tensor-derived quantities with implications for group analysis," tech. rep., Department of Statistics, University of Wisconsin, 2006.
28. H. Van Der Vaart, "Some results on the probability distribution of the latent roots of a symmetric matrix of continuously distributed elements, and some applications to the theory of response surface estimation." Report issued by the Institute of Statistics, University of North Carolina, 1958.